Sky imagery forecasting for renewable solar energy

-- Energy Science – Master Thesis --

Name: Cas Luuring
Emailadres: c.j.f.luuring@studens.uu.nl
Student number: 3715809
Date: 15/10/2015
Supervisor: B, Elsinga MSc

Universiteit Utrecht

5441 Words
(Without headings, table or references)

Table of Content

1. Executive Summaries

1.1.Executive Summary English

The number of photovoltaic (PV) installation has grown significantly in the past decades. However, the electricity generation from solar energy sources is not as stable as the conventional forms of electricity generation, due to seasonality and deviations in production and load profiles of solar resources. This combination poses technical challenges for the infrastructure of the energy market and strengthens the need for more accurate modeling, forecasting and prediction of solar radiation. In this paper a method for short term cloud forecasting has been developed using a ground-based sky imager at the University of Utrecht. Sky images taken every 30 seconds were processed to determine cloud coverage using a clear sky library. Cloud motion vectors were generated by cross-correlating consecutive images. Allowing the forecast of cloud coverages over forecast horizons of up to 5 minutes. There is much cloud detail that can be acquired, which will be far more difficult to achieve using alternative forecasting methods, such as numerical weather prediction (NWP) and satellite forecasting. The results showed that the average forecasted advection was approximately twice as good as the persistence. This shows great potential as further improvements will allow the matching errors and cloud-advection-versus-persistence errors to further decrease.

1.2.Executive Summary Dutch

Het aantal zonnecel installaties is het laatste decennia significant toegenomen. Echter, is de elektriciteit generatie van zonne-energiebronnen niet zo stabiel als de conventionele tegenhangers, door seizoeninvloeden en afwijkingen in productie en belasting profielen van deze vorm van elektriciteitsopwekking. Deze combinatie levert technische uitdagingen voor de infrastructuur van de energiemarkt en versterkt de noodzaak voor betere modellering, prognoses en voorspelling van zonnestraling. In deze paper is een methode voor de korte termijn wolken voorspelling ontwikkeld met behulp van luchtfoto's genomen door een sky imager van de Universiteit van Utrecht. De luchtfoto's zijn elke 30 seconden gemaakt en worden verwerkt om de wolkendekking te bepalen met behulp van een clear sky library. Bewegingsvectoren van de wolken zijn gemeten door een kruiscorrelatie te maken van opeenvolgende beelden. Dit bewerkstelligt de voorspelling van de wolken dekking met een voorspellingsperiode tot en met 5 minuten. Er is veel detail uit de wolken verkrijgbaar met de sky imager, wat veel moeilijker te realiseren valt met behulp van alternatieve voorspellingsmethoden, zoals numerieke weersvoorspelling (NWP) en satelliet voorspelling. De resultaten uit deze studie toonden aan de de gemiddelde voorspelde advectie ongeveer twee keer zo goed was als de persistentie. Dit toont aanzienlijke mogelijkheden als verbetering het verschil tussen errors tussen advectie en persistentie verder weten te verlagen.

2. Introduction

"If you have to forecast, forecast often." – Edgar Fiedler

The 1990s has seen a restructuring in the way the electricity was generated. Electricity generation used to be adjusted to match its current demand and generation was dominated by hydro-power, fossil and nuclear generation (West et al., 2014). However, the energy market has seen a paradigm shift with the rise of demand-side participation, due to the proliferation of large and correlated loads, the advent of the smart grid and a rise in renewable energy sources (Rahimi and Ipakchi, 2012). The changes in the energy market, through the active involvement of the demand-side generates a bidirectional flow of power, which in its turn requires a bidirectional flow of information between consumer and power system operators (Rahimi and Ipakchi, 2012).

The last decades have seen a rapid increase in electricity generation from renewable energy sources, such as solar energy. The number of photovoltaic (PV) installation has grown significantly, with a global cumulative installed capacity of over 138 GW in 2013 (EPIA, 2013). However, the electricity generation from solar energy sources is not as stable as the dominant forms of electricity generation, due to seasonality and deviations in production and load profiles of solar resources. The variability of solar resources causes increase in power losses due to differences between expected power production and actual power production, also known as mismatch losses (Picault et al., 2010).

The more active involvement of the demand side of the energy market and the rapid development of PV installations in combination with its variable nature poses technical challenges for the infrastructure of the energy market. These problems strengthen the need for more accurate modeling, forecasting and prediction of solar irradiance in order to minimize the mismatch losses and for Independent System Operators (ISOs) to properly balance the grid to ensure quality of supply and stability (Diagne, Lauret and David, 2012).

There are several techniques when trying to forecast the performance of solar renewable energy sources. These different techniques work best on different forecast horizons and geographic scales, where smaller forecast horizon often also means smaller geographic scale. Satellite techniques and Numerical Weather Programs (NWP's), which are statistical/data-driven approaches, cover the greater forecast horizons ranging from hours to 10 days and geographic scales reaching up to 10.000 km^2 (Sayeef et al., 2012). One of the techniques used for forecasting solar resources on small time scale and geographic scale is called sky imagery. The sky imagery technique uses cameras, often with a fish-eye lens, to capture images of the sky. This is either a camera facing the sky or a Total Sky Imager (TSI), which has a camera facing downwards onto a mirror. Some sky imagers have an extra mount attached that obscure the direct sunlight from the sun. These sky imagers can be used to identify clouds and track the movement of these clouds (Feister et al., 2000). The sky imagery technique can forecast the solar resource on a short time scale, as the geographic scale of the TSI lies within the range of 1 m^2 to 10 km^2 and the forecast horizon ranges of 1 to 20 minutes (Sayeef et al., 2012).

Some studies have already been conducted on short-term solar radiance forecasting through sky imagery. One of the most extensive and accurate research done is by The University of California, San Diego (UCSD). Which has an TSI installed that has taken images of the sky over UCSD since August 2009 (Chow et al., 2011). Despite shortcomings through

obscuration of the image by cloud deformation, evaporation and condensation, the UCSD was able to correctly nowcast, i.e. a term for forecasting within a six-hour timeframe, 70% of the time. As this study shows the potential of short-term irradiance forecasting and is very extensive in the explanation on its algorithm, it will therefore be used as a guideline for this study.

This study will focus on short-term irradiance forecast using this sky imagery technique. An initial setup has been developed at the University of Utrecht since 2013. The sky imager is located on the Hans Freudenthal Building of the university. The University of Utrecht is also involved in the SF&SG (Solar Forecasting & Smart-Grid) project, which oversees measurements of 202 PV cells installed at various locations within the province of Utrecht. This has great research potential, as we can see how well the short-term irradiance forecast does over greater distances. The research question that this study aims to answer is:

How accurate can we forecast the short-term renewable solar energy source by using sky imagery at the University of Utrecht at short and longer geographical range?

This research question will be answered by answering the following sub questions:

1. *Can we create a model, which will be able to accurately predict renewable solar energy source in retrospect for the location of the University Hans Freudenthal Building?*

2. *What will be the effect on the accuracy of the forecast when the geographical scope is broadened?*

This paper is structured as followed: Section 3 will cover the method, where the explanation of experimental setup and methods for the algorithm will be given. In section 4 the results will be elaborated. In section 5 the discussion of the paper will be shown. This research will end with section 6, which contains the conclusion of the research, and section 7; the reference list.

3. Method

The following section covers the setup for the sky imager, the methods used for setting up the clear sky library, cloud detection, cloud classification, cloud tracking and finally the shadow mapping.

3.1. Experimental setup

On the rooftop of the university Hans Freudenthal Building (at 52.087781°N, 5.167473°E) a sky camera has been installed since 2013. The SRF-02 All-Sky Camera, by EKO instruments, is set up to take pictures of the sky with a resolution of 1600 by 1200 pixels. It takes pictures every 10 minutes starting from 07:00 in the morning till 16:20 in the afternoon. For every 10 minutes two pictures are taken, each one having a different shutter speed to create a broader dataset. For experimental purposes the sky imager will also take pictures every 30s for four specific dates, to give a more detailed dataset. Next to the sky camera are several PV installations set up in a parallel setting, each with their own volt and power measuring devices. Alongside of the PV installations a thermometer, pyrheliometer and pyranometer are installed, measuring the temperature, the Direct Normal Irradiance (DNI) and Global Horizontal Irradiance (GHI) respectively. Furthermore, the University of Utrecht is collaborating with DNV GL and Ecofys in the Solar Forecasting & Smart Grid (SF&SG) project overseeing measurements 202 PV systems. These PV systems are installed at various locations within the range of the Province of Utrecht, as can be seen in Figure 1.

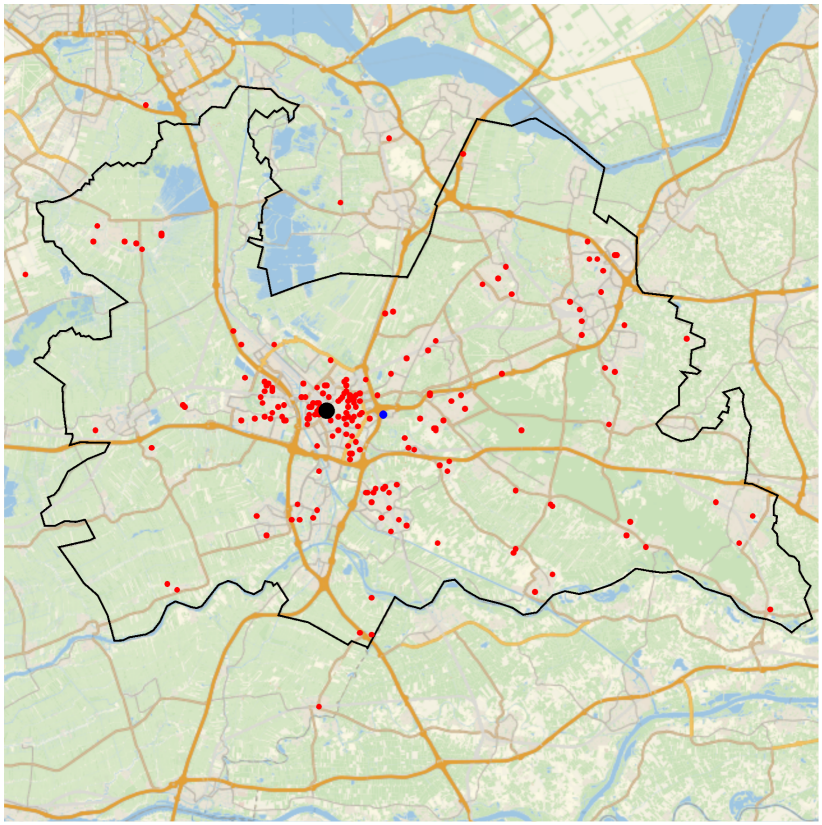

Figure 1. Map of the province of Utrecht with Utrecht (black), Sky Imager (blue) and all locations of the PV installations overseen by SF&SG (red) created with Mathematica

The next sections will cover the methodology of the algorithm, which will be used for forecasting the short-term irradiance. A schematic overview of methodology used in this paper can be found in Figure 2.

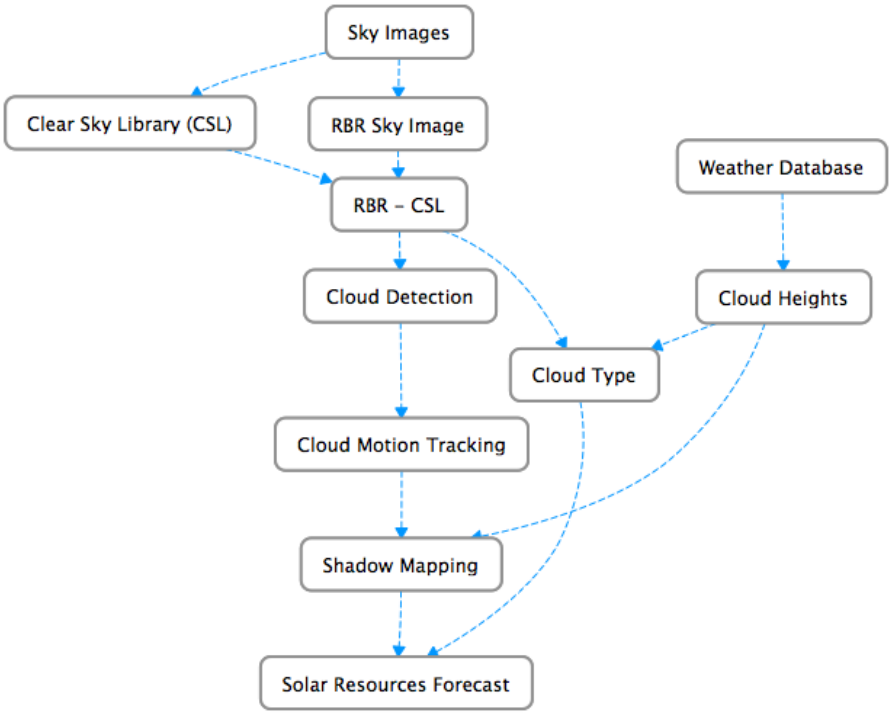

Figure 2. Schematic overview of the methodology of the algorithm used for irradiance forecasting

3.2.Image acquisition

The images are acquired from the sky camera on the roof of the Hans Freudenthal Building. Raw image output, as seen in Figure 3**,** is used before processing is conducted. First a mask is subtracted from the images covering for antenna's and other objects on top of the building, which are obscuring the view of the sky in the picture. Subsequently the image is cropped to a rectangular shape, discarding all the black area on the sides. Lastly, the blacks in the image are removed resulting in the picture as seen in Figure 3.

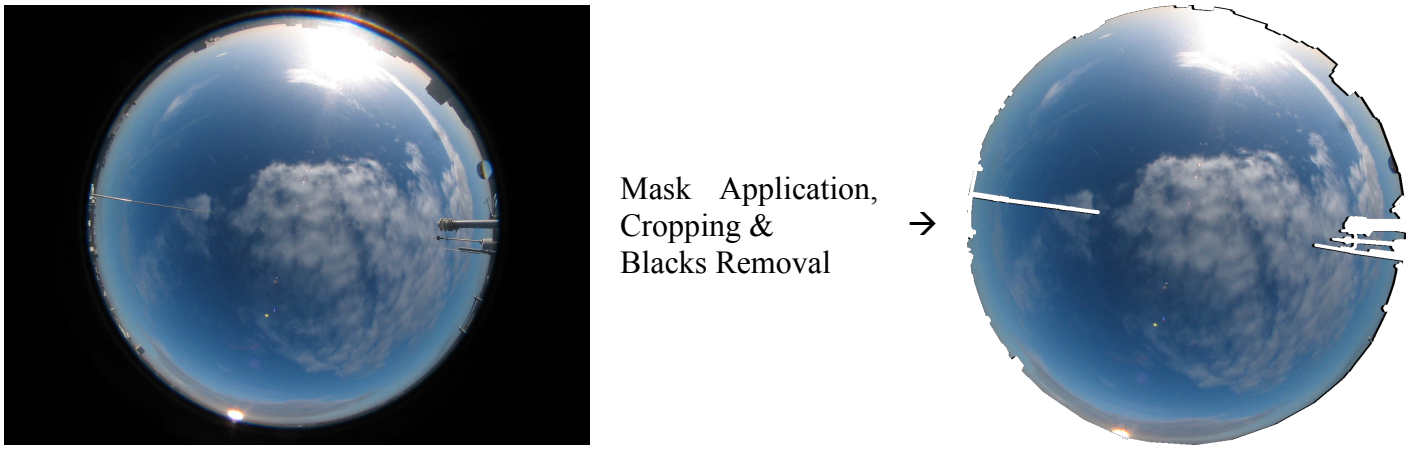

Figure 3. Transformation of the raw image (left) to the first processed image (right)

The observation of clouds within the picture is based on the ratio between the red and the blue channel. This method is used, due to the fact that Rayleigh scattering of the visible wavelengths is done more evenly by clouds than clear sky (Shields et al., 2009). This therefore enables the computer to make a better distinction between clouds or clear sky. The initial image is converted into a dataset with a red-blue-ratio (RBR), as can be seen in Figure 4.

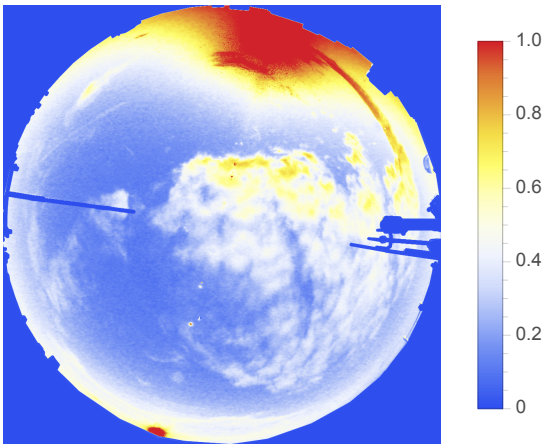

Figure 4. Colorized image of the red-blue-ratio dataset

3.3. Clear sky library

The RBR of an image with the sky imager is not uniform, this is due to the relative distribution of aerosol. A Clear Sky Library (CSL) is created to generate a picture of clear sky at any moment in time, using the date as input parameter. This CSL is based on research from Shields et al. (2009) and will be used as a threshold which will account for cloud pixels illuminated by the sun within the sun circle, an approximate 20° field of view centered on the sun position. It is very useful for better defining the clouds and eliminating the effect of the sun and aerosol on the image RBR.

The images used for the CSL are found by letting an algorithm search for moments of clear sky through the image database using reference images of clear sky, which where handpicked throughout different dates in the year. The algorithm scans through the dates of the pictures and finds the corresponding solar position. The algorithm then compares the solar position and distribution of the red and blue channel of all the pictures in the image database with the solar position and distribution of the red and blue channel of the reference images to find all

clear sky images. After these images are converted to RBR datasets, a regression is made between the sun-pixel-angle and the zenith angle (ZA). This finalizes the creation of the CSL.

The CSL can now be used to generate an image RBR of clear sky at any given point in time, only a date is needed as input variable. The algorithm then searches for a dataset within the CSL with a ZA closest to the ZA of the given date. From this matching dataset the image RBR of the clear sky is generated.

3.4.Cloud mapping

To assign for the image distortion created by the fisheye properties of the lens of the sky imager an algorithm is created. This algorithm uses a forward calculation to assign each pixel to its appropriate position in the mapped image. The forward mapping used for assigning each of the pixels is based on:

$$f(r) = CloudHeight * \tan(\sin^{-1}\frac{r}{R})$$

This forward mapping is depicted in Figure 5. For this forward mapping r is equal to the pixel distance from the center and R is equal to the radius pixel distance of the fisheye lens image. The Arcsine of r/R gives the angle of α, which in its turn can be used to calculate the appropriate position x for any pixel. This mapping is applied to all the processed images.

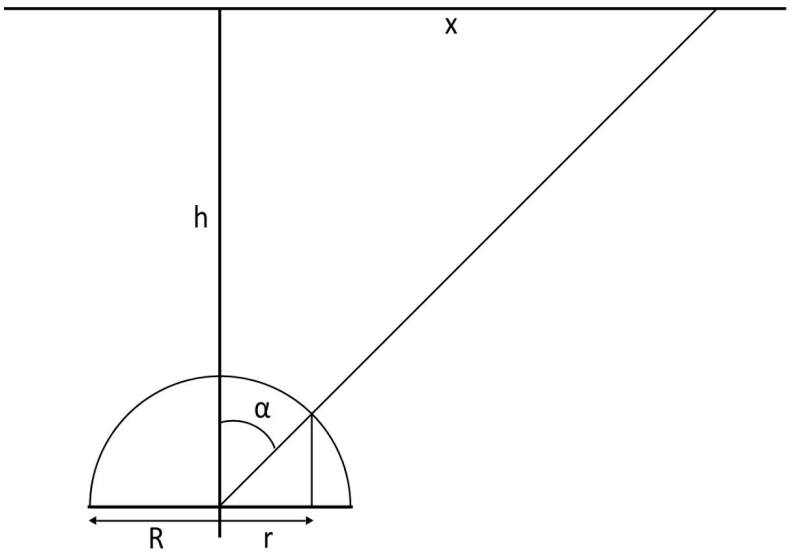

Figure 5. Representation of the cloud map as captured by the sky imager

3.5. Cloud detection

Once the RBR of the CSL is defined, it will then be used together the RBR of the current image to define a final image of the clouds. From here the cloud fraction is computed, being the number of cloudy pixels divided by the total number of pixels (Pfister et al., 2003). This cloud image is used in further sections to classify the clouds and enable cloud tracking. The clouds are further defined by using Wolfram Mathematica code that identifies the cloud as objects.

3.6. Cloud classification

Cloud classification is an important factor, as the effect that clouds can have on the reflection and absorption of solar irradiance is influenced by their shape, size and composition (Buch, Sun and Thorne, 1995). The classified cloud condition will therefore influence the calculation done in the following sections. The method defined by Buch, Sun and Thorne (1995) will be applied when classifying the clouds using images from the sky imager. The definition of the different sky condition classes, as seen in Table 1, are used following the research of Lui et al. (2011).

Table 1. Sky condition classes following the research of Lui et al. (2011)

Sky condition classes	Description
Cirriform	Thin clouds; very wispy and feathery looking
Cumuliform	Thin or thick clouds occurring in sheets or pathes with wavy rounded masses or rolls
Stratiform	Horizontal, layer clouds that stretch out across the sky like a blanket
Clear	Clear sky

These cloud conditions will be correlated to the measured DNI from the installed pyrheliometer to give an idea of the influence of the sky condition on the solar irradiance captured on the surface.

3.7. Cloud tracking and forecasting

From the cloud detection section, the clouds are identified, mapped and then tracked. The algorithm uses a technique called; speeded up robust features (SURF), to specify distinct pixels in the clouded area of the image at t_0 (Bay et al., 2008). These distinct pixels are then tracked in the subsequent images, the displacement of the pixels is then translated into a motion vector plot. The research done by Jayadevan et al. (2012) stood as a guideline for the creation of this algorithm. The vector plot is then translated into the displacement of the cloud pixels in the forecast cloud map.

Binary cloud images are used to check the accuracy of the algorithm. The forecasted cloud image is compared to the actual cloud image to identify the matching error between the forecasted cloud map and the actual cloud map, the definition as given in Chow et al. (2006) is used:

$$e_m = \frac{P_{false}}{P_{total}} * 100\%$$

The matching error (e_m) is defined as the ratio between the total number of pixels falsely predicted (P_{false}) and the total number of pixels (P_{total}). Furthermore, the cloud-advection-versus-persistence (cap) error from Chow et al. (2006) is used to see whether advection gives a better accuracy of the cloud map compared to persistence, being the original image without movement. The formula used for this error cap is

$$e_{cap} = \frac{e_m}{e_{m,p}} * 100\%$$

Here the matching error (e_m) is compared to the matching error of the persistence cloud map ($e_{m,p}$). A $e_{cap} > 1$ will imply that the persistence cloud map gives a better forecast.

3.8. Shadow mapping

After the clouds are detected, classified and tracked, the cloud height is determined. The vertical distribution of clouds determines where the shadow projection of the cloud hits the surface (Kleissl, 2013). A ceilometer is used to determine the altitude of the cloud base height. Although, no such device is present at the UPOT testing site, the testing site The Bilt of the the Royal Netherlands Meteorological Institute (KNMI) has such a device present. Testing site number 261 (The Bilt) is situated approximately 1.5 km from the location of the UPOT sky imager. Their database is incorporated in the WeatherData function of Wolfram Mathematica and can therefore be easily implemented into the solar forecasting algorithm. The relation of the cloud height to the range of the is given with the following formula:

$$Range\ Shadow\ Map = \tan(\frac{FOV}{2}) * Cloud\ Heigth * 2$$

In this formula, FOV is the field of view, meaning the span of the fisheye camera in degrees. For the positioning of the shadow mapping a method called ray-tracing is used. This method is adopted from earlier research on solar energy forecasting done by Urquhart et al. (2013). The method determines the positioning of the cloud map by tracing rays along the solar vector. The solar vector is defined using the position of the sun at the date the cloud map was taken. This cloud map is then projected on the map of Utrecht as can be seen in Figure 18.

3.9. Reliability and validity

The image database is established from 2013, however from end 2013 until July 2014 the area around the sky camera was under constructions and a crane was obstructing the view, these dates are therefore exempted from use. The images with image capturing interval of 5 minutes are only used up to section 5.8. The methods used in the research done by Chow et al. (2011) and Pfister et al. (2003) on short-term irradiance forecasting with sky imagery are used as reference and ensure the validity of this study.

4. Results

4.1. Selected Dates

For the results in sections 5.2 until 5.8 the complete database of images was used. The interval between the pictures was shortened on the following days: October 26, 2015; December 04, 2015; December 08, 2015 and December 09, 2015. For these days the sky imager was set to take a picture every 30 seconds and these days are assessed to find the accuracy of the sky imagery forecasts. These pictures were used from section 5.9 onwards.

4.2. CSL

The CSL is created from images selected by an algorithm that searches for clear sky days. The algorithm uses reference images and compares the distribution of the red and blue channel with other images to conclude if the image at hand is of a clear sky. The algorithm returned approximately 500 clear sky images, which were converted to CSL datasets. From these 500 datasets with different dates and times the best matching one is chosen for the CSL image generation. These image were then converted to RBR images giving the ratio between the red and blue channel.

These RBR images were then all converted to CSL datasets. This was done by determining the position of the sun in the image. From that point the image RBR was gradually deconstructed, by taking the values of incremental distance from the position of the sun. An example of such a dataset can be seen in Figure 6.

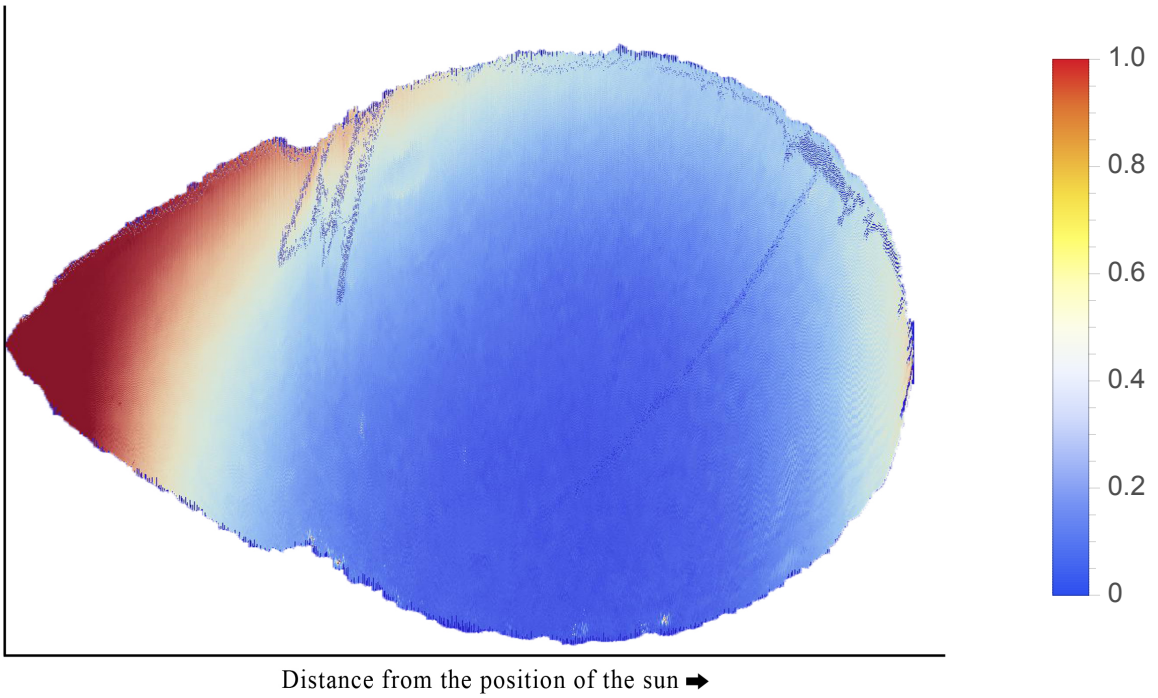

Figure 6. Colorized image of a CSL dataset

From Figure 6 can be seen that clear sky images have a rather uniform RBR distribution. The closer to the sun the higher the values of the RBR, this is due to the forward scattering of sunlight which makes the circumsolar area brighter. At the right of Figure 6 the RBR values go up again due to increased Mie scatter caused by the higher aerosol concentration at the

horizon. The imperfection which can be spotted in Figure 6**,** working downwards from the top, are caused by the obstructions in the image, such as antennas and other measuring devices, but will be excluded when generating the CSL RBR images.

The clear sky library now consists of a library with over 500 of these datasets, which enables the generation of a CSL RBR at any given date and time. In Figure 7 such a CSL RBR is generated for 26 November, 2015 at 11:59:30 with a corresponding position of the sun with a azimuth of 172.95 degrees and an zenith angle of 73.28 degrees.

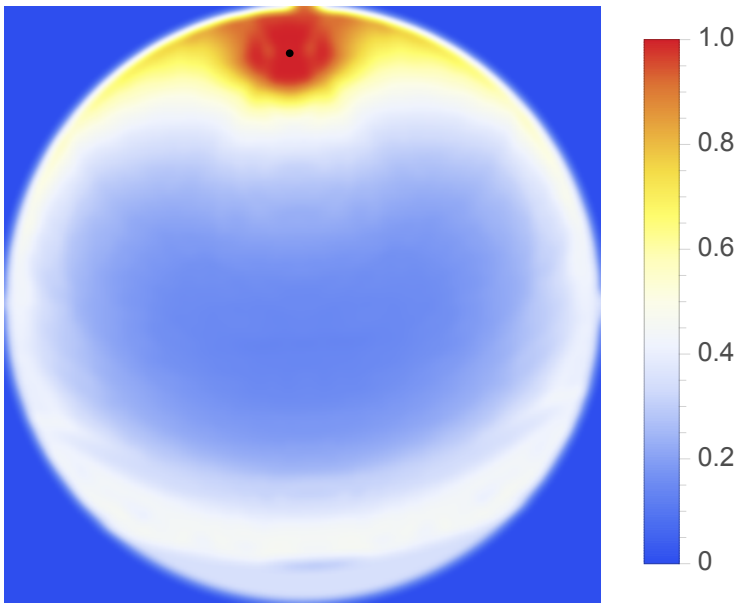

Figure 7. Colorized image of a generated RBR image of 26 November 2015 at 11:59:30 with the position of the sun (black)

4.3. Cloud Mapping

To account for the effect of the fisheye properties of the sky imager a forward mapping is used, as described in the previous chapter. The amount of pixels needed for the forward mapping increases as r/R increases (see Figure 5), therefor the mapping is set to an angle of 70 degrees leaving a field of view of 140 degrees. Setting the field of view to 140 degrees increases the accuracy of the mapping, while at the same time eliminating the problem of misclassification of the thicker clouds near the horizon. The thick clouds are often misclassified due to the higher aerosol concentrations and the quickly diminishing amount of pixels near the horizon.

All the parameters for the forward mapping were calculated from taking pictures with the sky imager of a checkerboard. The points of the checkerboard in all the images were then calibrated, which resulted in the final parameters of the mapping. The influence of the mapping on one of the checkerboard images can be seen in Figure 8.

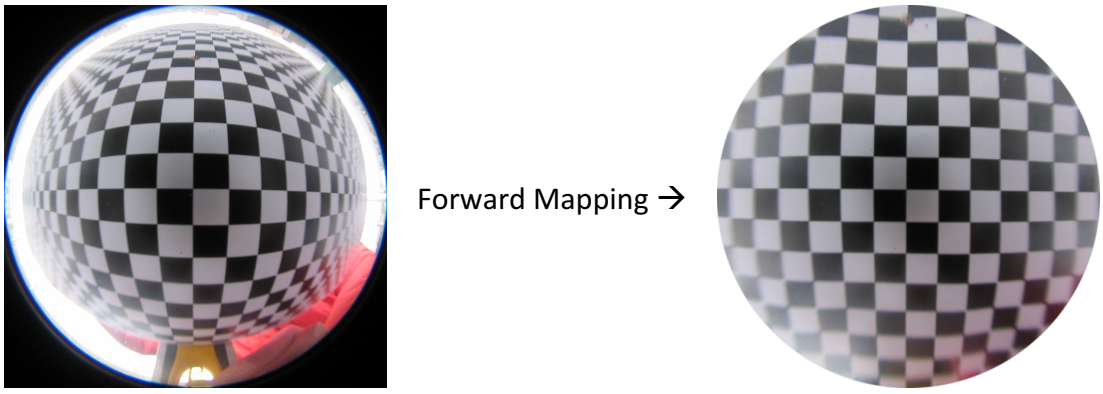

Figure 8. Example of the forward mapping applied to a checkerboard image

As can be seen in Figure 8 the distortion caused by the fisheye properties of the sky imager is neutralized. The same is done for all the pictures which were processed to better define their real size and shape. An example of the forward mapping can be seen in Figure 9.

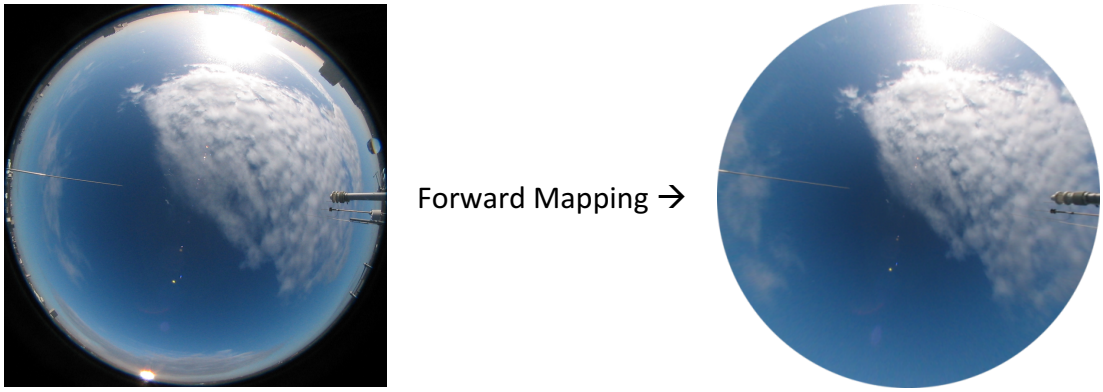

Figure 9. Example of the forward mapping applied to a cloud image

From Figure 9 can be seen that the shape of the clouds in the initial image is slightly changed. The neutralizing of the fisheye properties of the sky imager causes cloud in the center of the image to shrink compared to the clouds at the edges which will enlarge.

4.4. Cloud Detection

After the generation of a CSL RBR image and mapping of the images, the difference-RBR is created. This is the difference between the generated CSL RBR image and the current RBR image, negating the influence of the sun and the higher aerosol concentration near the horizon. Thus better defining the clouds in the image enabling the detection of solely clouds. The difference RBR is then converted to a binary image, converting clear sky into values of zero and clouds into values of one. These steps can be seen in Figure 10.

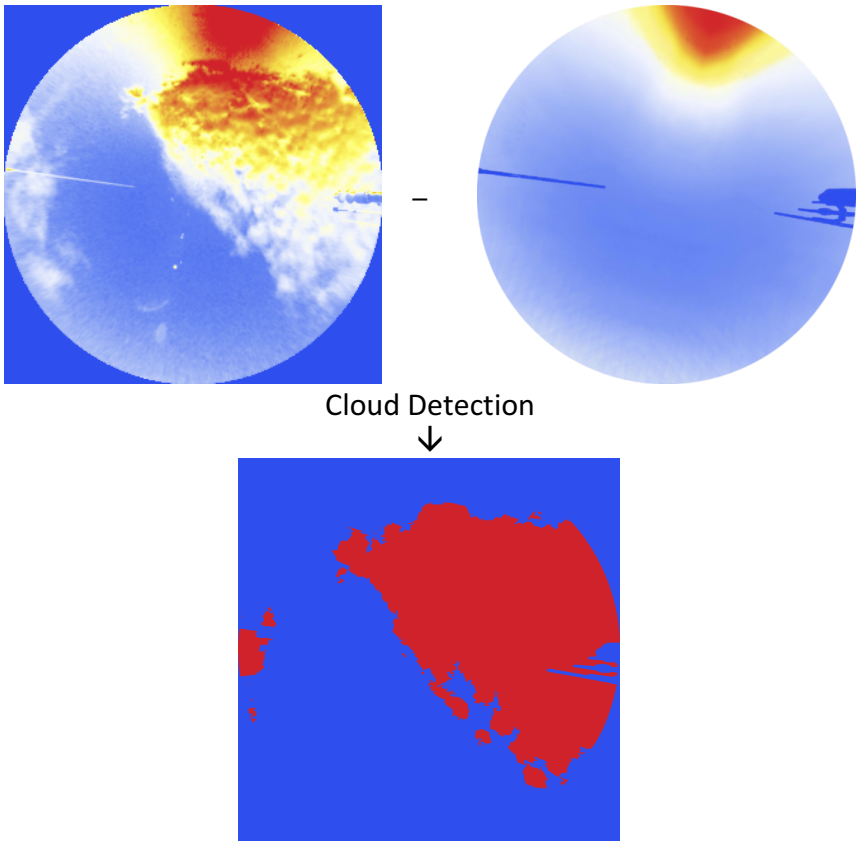

Figure 10. Example of an image CSL subtracted from an image RBR (top left) followed by the cloud detection algorithm resulting in a binary image of cloud (blue)/clear sky (red)

4.5.Cloud Detection Validity

The validity of the cloud detection can only be assured visually; this section will therefore describe qualitatively how well the cloud detection algorithm is functioning. In general, the method used by the algorithm works well for well defined opaque clouds most of the time. However, optically thin clouds are sometimes misclassified as clear sky. This is due to the fact that clear sky is visible through these kinds of clouds and therefore the algorithm defines them as being clear sky. This is a problem which occurs often in solar forecasting using sky imagery (Shields et al., 1998). Furthermore, near the sun and the horizon thicker clouds are sometimes misclassified as clear sky, due to high influence of the sun. This is the main problem of the sky imager used in this study as compared to a total sky imager with sun obscuration devices used in other solar forecasting research; Chow et al. (2006), Pfister et al. (2003) and Ghonima et al. (2012).

4.6.Cloud Height

From the databases constructed by Wolfram Mathematica and KNMI the cloud height determined. The cloud height is essential for generation of the shadow map explained in the previous chapter. An overview of the cloud heights for 2015 is given in Figure 11.

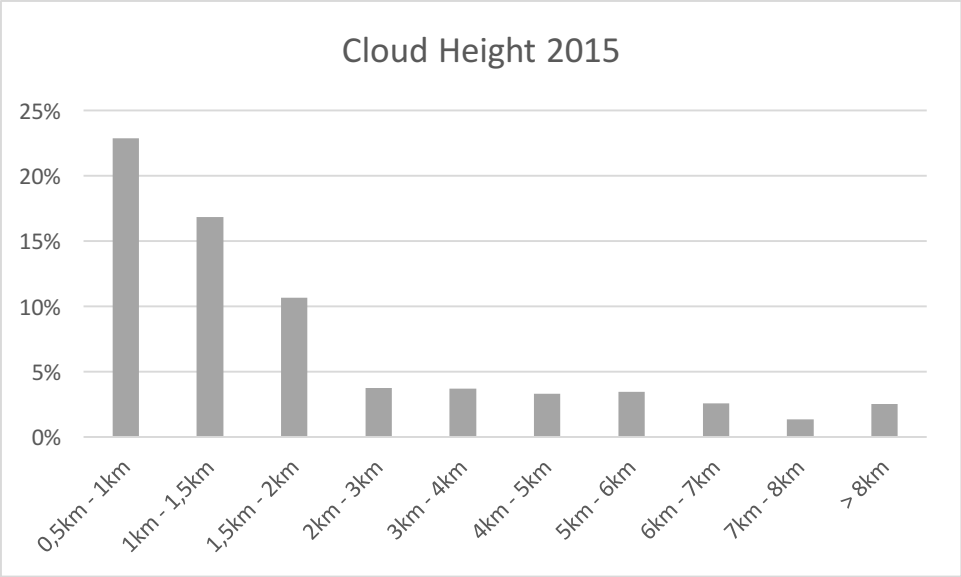

Figure 11. Histogram of the distribution of the different cloud heights measured in 2015

From the data on cloud heights can be seen that the cloud height ranges from zero to ten kilometers. The cloud height is an essential parameter on the outcome of the shadow map as it determines its range. In the previous chapter the formula of the range of the shadow map was defined, using this formula we can conclude the diameter of the shadow map falls in between approximately 5 km for low clouds with a height of 1 km and 44 km for clouds with a height of 8km. Figure 12 show the map of Utrecht with the different shadow map ranges and the distribution of the range.

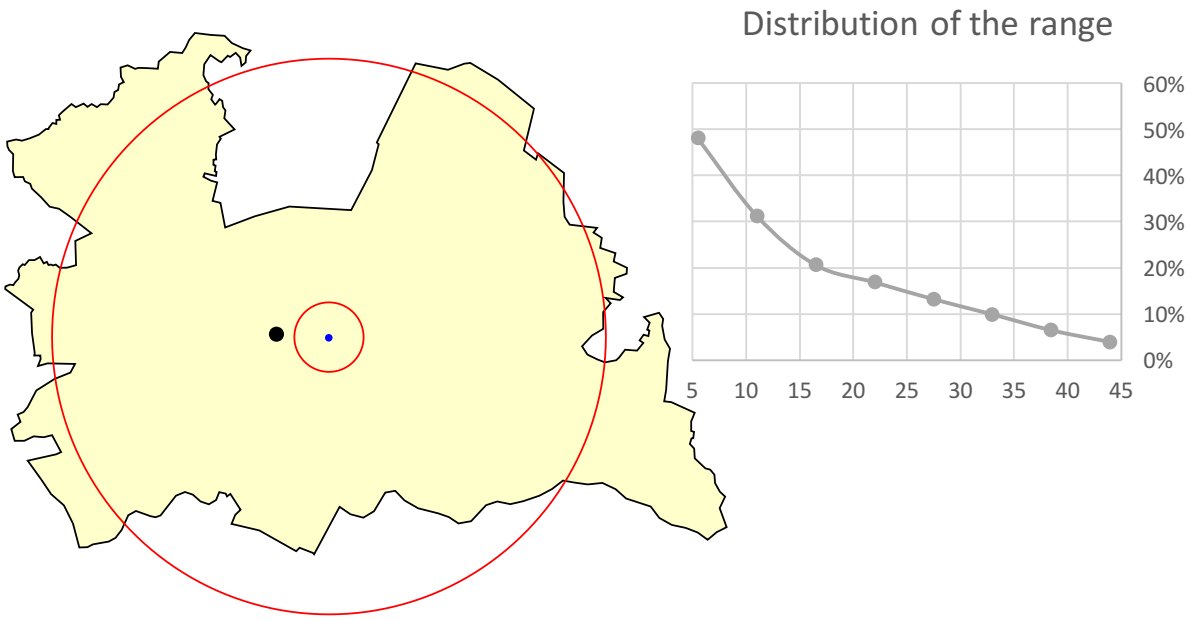

Figure 12. Mapped ranges with cloud height 1km and 8km and the distribution of the ranges in km with Utrecht (black), Sky Imager (blue)

From the distribution of the range in Figure 12 can be spotted that almost half of time the range of the cloud map is above 5km. This can give a good indication of how many cameras would be needed if all 202 PV installation overseen by the University of Utrecht would need forecasting. Overlapping sky imagery would also come with the extra advantage that cloud

base heights can by be calculated very accurately for specific clouds (Seiz, Baltsavias and Gruen; 2002).

4.7. Cloud Classification

The classification of the clouds is an essential part of the solar radiation going through the clouds. As different clouds have different properties when it comes to reflecting and absorbing light. The classification was determined by comparing elongation and shape of the clouds. Furthermore, a comparison between reference images with the cloud types already classified and the cloud images was made. Lastly the cloud heights were compared to the cloud classification, as different cloud types occur at different heights. Therefore, this enables the excludability of cloud types at specific cloud heights. Figure 13 shows the results of the occurrence of different cloud types in 2015.

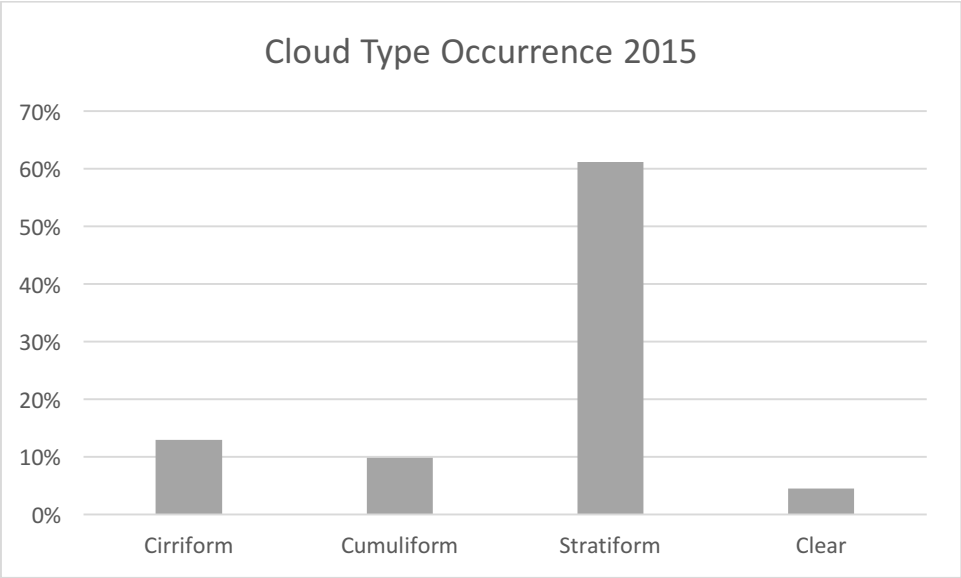

Figure 13. Histogram of the different cloud types measured in 2015

4.8.Cloud Coverage

From the cloud detection section an overview of the cloud cover fraction of 2015 is given at a field of view (FOV) of 140 degrees. The cloud cover fraction is the total amount of pixels identified as cloudy divided by the total amount of pixels in the picture. With cloud cover fraction being equal to one describing full coverage of clouds and being equal to zero meaning a clear sky. Figure 14 shows the results of the cloud cover fractions found in 2015.

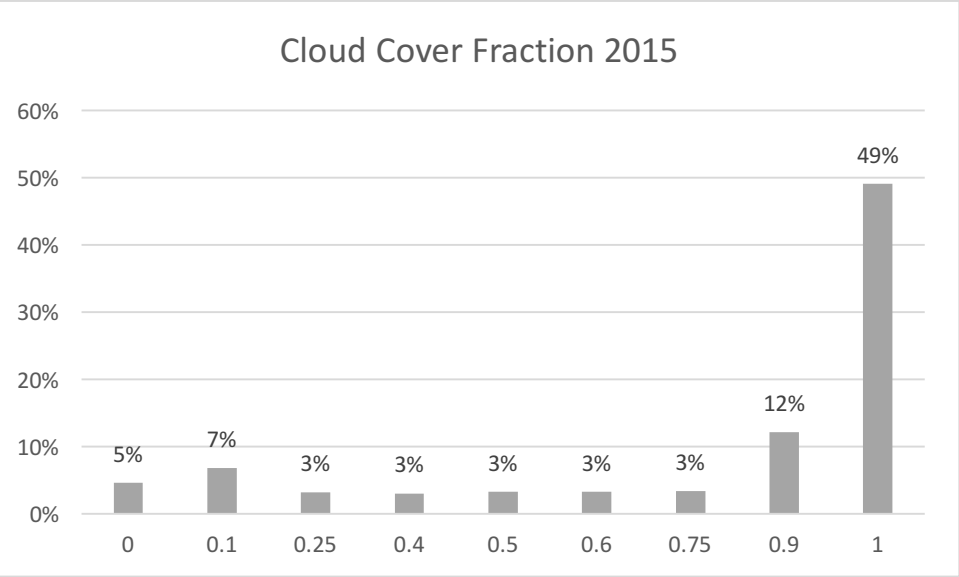

Figure 14. Histogram of the different cloud cover fraction measured in 2015

From Figure 14 can be seen that the weather in Utrecht is often cloudy as only five percent of the weather was identified as being clear sky. 49 percent of the time the cloud coverage was equal to one, meaning total cloud coverage. When the cloud coverage is equal to zero or equal to one, solar radiation forecasting has no use. However, approximately 50% of the time this is not the case and solar forecasting can have a substantial use for our location.

4.9. Cloud tracking

From this section onwards only the images from the selected dates with an image capture interval of 30 seconds are being used. For the cloud tracking first the binary image of the clouds is used. This image is processed using the SURF method as described in the previous chapter. From there the most important cornering points of the image features are selected. This can be seen in Figure 15, where a binary image of the clouds is shown with the most important corner sections depictured as red dots.

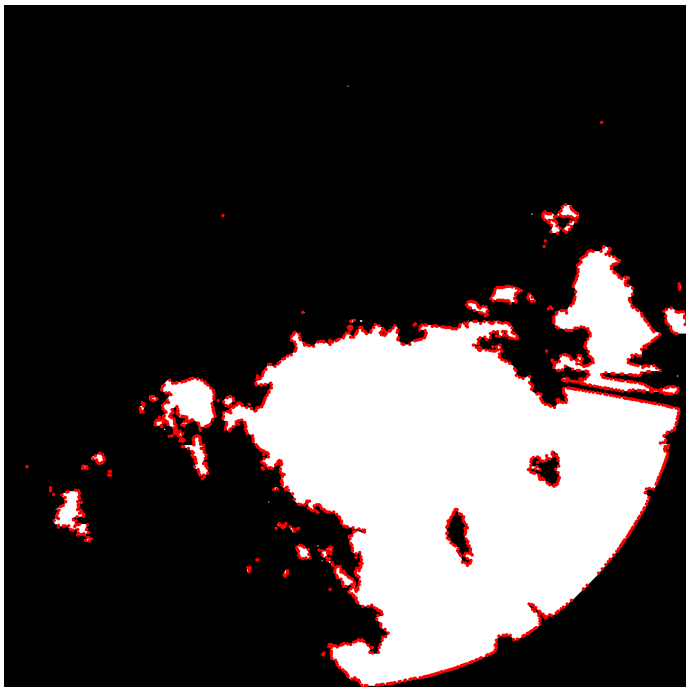

Figure 15. Example binary cloud image with SURF tracking points (red)

The points are then used for tracking the subsequent images. From the tracking the missing points were eliminated. Furthermore, the tracking points with a direction with two standard deviations from the mean were seen as outliers and were discarded, leaving only the accurate vectors. This process can be seen in in Figure 16, which shows an image of t_0 with vector plot t_{0+30s} before and after the elimination of the the inaccurate vectors has taken place.

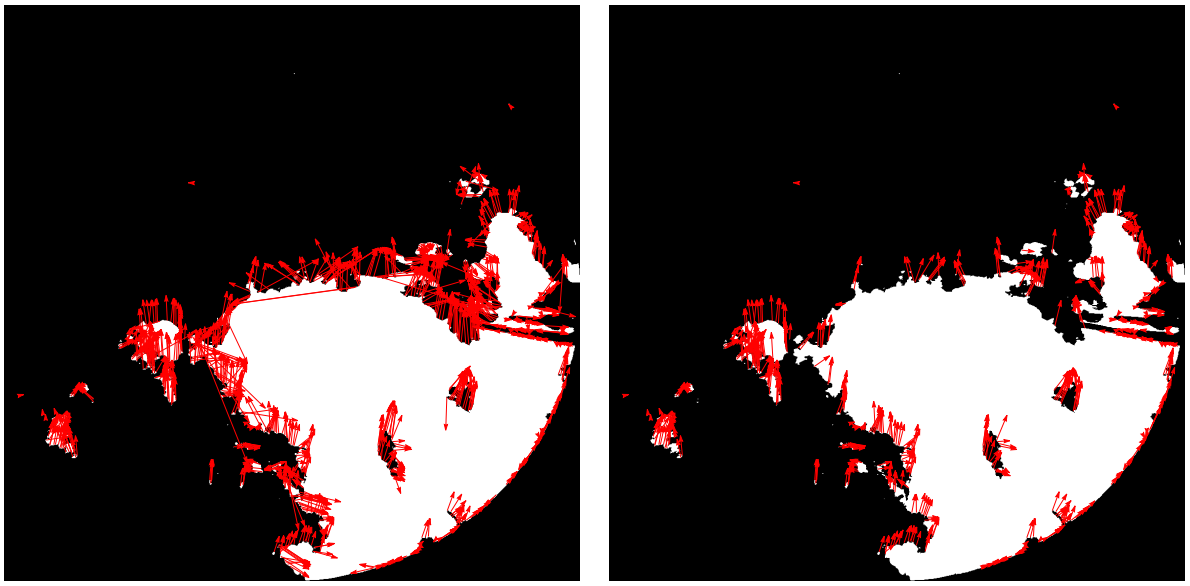

Figure 16. Example of the vectors measured (left) and the exclusion inaccurate vectors

From the vector plots depicted in the second image of Figure 16, an average uniform vector is defined which is used in the advection of the t_{0+30s} image. The same is done for all subsequent images as well for the images with intervals from 30 seconds to 5 minutes.

4.10. Forecast results

From the previous sections data is collected which will be used to forecast the cloud maps. A comparison is made between the original cloud map (persistence), the original cloud map including advection and the real cloud map. From here we can tell whether or not pixels are forecasted correctly, but also if the cloudy pixel should have been a clear pixel or vice versa. An example can be seen in Figure 17.

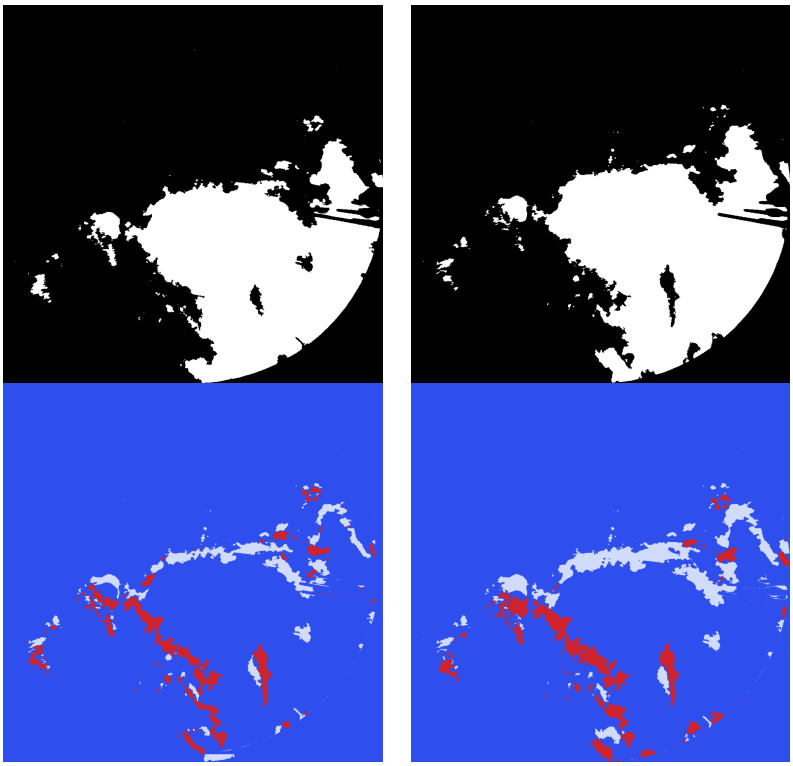

Figure 17. Example of cloud movement cloud map t=0 (top left) and t=30 (top right) and the forecasting results of advection (bottom left) and persistence (bottom right); where dark blue is correctly forecasted pixels, light blue is forecasted clear sky but actually cloudy and red is forecasted cloud but actually clear sky.

The following results for the selected dates is acquired using the algorithm as described above. Starting with an overview of the mean of e_m and the mean of e_{cap}, as described in the previous chapter.

Table 2. Measured matching errors and cap errors for selected days

Forecast horizon	*Mean of e_m*	*Std. of e_m*	*Mean of e_{cap}*	*Std. of e_{cap}*
30s	5.0%	5.5%	68.3%	11.9%
60s	9.5%	5.5%	67.1%	12.8%
90s	9.3%	6.2%	65.5%	15.5%
120s	10.9%	6.2%	64.5%	12.9%
150s	12.2%	6.5%	62.0%	13.9%
180s	13.6%	6.4%	59.5%	13.4%
210s	15.1%	6.8%	58.4%	12.8%
240s	15.9%	7.2%	56.7%	11.5%
270s	16.3%	7.2%	53.9%	11.5%
300s	16.9%	7.7%	51.3%	12.3%

The results acquired from the algorithm show that on average the cloud advection improves the forecast compared to the persistence. The matching error obtained over longer forecasting horizons increases, but this can be expected as longer forecasting periods encounter more uncertainties. Moreover, part of the selected days encountered strong forms of cloud deformation, formation, or evaporation. Due to the small sample size of this study, exclusion of these types of deformation was not suitable.

4.11. Shadow maps

From the binary cloud images, shadow maps were created. These depict were shadow will be casted on ground level. Figure 18 shows the location of the shadow map of the cloud highlighted by the yellow disk. This shadow map was created for 26 November, 2015 at 10:18:35, the corresponding position of the sun has an azimuth angle of 149.2° and a zenith angle of 78.3°. As can be seen from Figure 18 the position of the binary cloud image is located northwest of the UPOT imagery site.

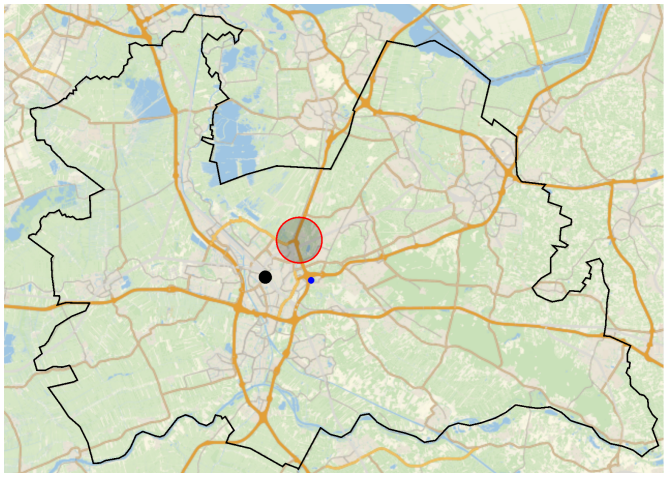

Figure 18. Location of the shadow map for 26 November, 2015 at 10:18:35 on the map of the province of Utrecht, with Utrecht (black) and sky imager (blue)

The output of the PV system located in this area could be correlated to the binary cloud map, however due to technical malfunction no data was collected in this. Therefore, at this moment this study will be unable to perform any analysis on the accuracy of the cloud map and will have to wait for new data to arrive.

5. Discussion

Despite the fact that this research is performed with great care, it has limitations. The sample space of the four days is limited and accuracies achieved from the algorithm are therefore not yet conclusive and will need more testing. Moreover, during the four selected days different forms of cloud deformation, formation, or evaporation were encountered decreasing the quality of the sample space and its results.

Furthermore, this research was unable to generate any analysis on the output of the shadow maps as no data was available for any of the selected days. This was due to a malfunction of the data collection which stopped working from October 2015 onwards.

This research has showed promising outcome, which can be used in further research. The algorithm is a strong base to build upon, to further improve the accuracies of the forecasting and to analyze more data. Image with the 30 second interval can be processed and the validation of the shadow maps can be performed.

The initial set-up as used in this study can also be expanded, as more cameras will give a more accurate cloud definition and will allow for the calculation of cloud height using triangulation. Furthermore, it will allow for the simultaneous forecasting of the 202 PV installations from the Solar Forecasting & Smart Grid project.

6. Conclusion

The technique used for short term irradiance forecast using sky imagery was presented for four days at the University of Utrecht. The algorithm as described above shows much potential in forecasting solar irradiance at small forecasting horizons. There is much cloud detail that can be acquired, which will be far more difficult to achieve using alternative forecasting methods, such as NWP and satellite forecasting.

The foundation of the algorithm is solid as an extensive clear sky library has been created. This resulted in a database with over 500 datasets, allowing the algorithm to choose an appropriate reference dataset to generate the image CSL RBR from. Also the ranges of the shadow maps that were specified can be used as basis for determining how many cameras should be installed if more PV installed need to be forecasted.

The forecast was measured by observing the movement of the clouds, these can be tracked with good accuracy. From the results obtained we can see that the forecasting method has an added value. Despite the shortcomings mentioned above the average matching errors of 5.0% was found for forecasts for 30 seconds and a matching error of 16.9% for the forecast horizon of 5 minutes. The average cloud-advection-versus-persistence error of 68.3% for the forecast horizon of 30 seconds **s**how that on average the cloud advection method worked approximately 1.5 times better than the persistence method. For the forecast horizon of 5 minutes The average cloud-advection-versus-persistence error was 51.8% this means the advection was approximately twice as good as the persistence. This shows great potential as further improvements will allow the matching errors and cloud-advection-versus-persistence errors to further decrease.

7. Reference List

Bay, H., Ess, A., Tuytelaars, T., & Van Gool, L. (2008). Speeded-up robust features (SURF). *Computer vision and image understanding*, *110*(3), 346-359.

Buch, K. A., Sun, C. H., & Thorne, L. R. (1995, March). Cloud classification using whole-sky imager data. In of the 5th Atmospheric Radiation Measurement Science Team Meeting, San Diego, CA, USA (pp. 19-23).

Chow, C. W., Urquhart, B., Lave, M., Dominguez, A., Kleissl, J., Shields, J., & Washom, B. (2011). Intra-hour forecasting with a total sky imager at the UC San Diego solar energy testbed. *Solar Energy*, *85*(11), 2881-2893.

Denholm P, Margolis RM. Evaluating the limits of solar photovoltaics (PV) in traditional electric power systems. Energy Policy 2007;35(5):2852e61.

Diagne, H. M., Lauret, P., & David, M. (2012, May). Solar irradiation forecasting: state-of-the-art and proposition for future developments for small-scale insular grids. In *WREF 2012-World Renewable Energy Forum*.

European Photovoltaic Industry Association. (2013). Global market outlook for photovoltaics 2013–2017. EPIA Report.

Feister, U., Shields, J., Karr, M., Johnson, R., Dehne, K., & Woldt, M. (2000, November). Ground-based cloud images and sky radiances in the visible and near infrared region from whole sky imager measurements. In EUMP31, EUMETSAT Satellite Application Facility Workshop, Dresden, Germany (pp. 20-22).

Hanel RA. Radiometric measurements from satellites. Aerospace Engineering 1962.

Inman, R. H., Pedro, H. T., & Coimbra, C. F. (2013). Solar forecasting methods for renewable energy integration. Progress in energy and combustion science,39(6), 535-576.

Jayadevan, V. T., Rodriguez, J. J., Lonij, V. P., & Cronin, A. D. (2012). Forecasting solar power intermittency using ground-based cloud imaging. InWorld Renewable Energy Forum.

Jenkins, A. (2013). The Sun's position in the sky. European Journal of Physics,34(3), 633.

Kamthe A, Marquez R, Coimbra CFM, Cerpa A. Sub-minute solar irradiance forecasting using wireless sensor networks. Merced: University of California; 2011.

Kleissl, J. (2013). Solar energy forecasting and resource assessment. Academic Press.

Liu, L., Sun, X., Chen, F., Zhao, S., & Gao, T. (2011). Cloud classification based on structure features of infrared images. Journal of Atmospheric and Oceanic Technology, 28(3), 410-417.

Nguyen, D., & Lehman, B. (2008). An adaptive solar photovoltaic array using model-based reconfiguration algorithm. Industrial Electronics, IEEE Transactions on, 55(7), 2644-2654.

Pfister, G., McKenzie, R. L., Liley, J. B., Thomas, A., Forgan, B. W., & Long, C. N. (2003). Cloud coverage based on all-sky imaging and its impact on surface solar irradiance. Journal of Applied Meteorology, 42(10), 1421-1434.

Picault, D. (2010). Reduction of mismatch losses in grid-connected photovoltaic systems using alternative topologies (Doctoral dissertation, Institut National Polytechnique de Grenoble-INPG).

Rahimi, F., & Ipakchi, A. (2010). Demand response as a market resource under the smart grid paradigm. *Smart Grid, IEEE Transactions on*, *1*(1), 82-88.

Seiz, G., Baltsavias, E. P., & Gruen, A. (2002). Cloud mapping from the ground: Use of photogrammetric methods. *Photogrammetric engineering and remote sensing*, *68*(9), 941-951.

Sayeef, S., Heslop, S., Cornforth, D., Moore, T., Percy, S., Ward, J.K., Berry, A., Rowe, D., 2012. Solar intermittency: Australia's clean energy challenge (No. June).

Shields, J. E., Johnson, R. W., & Koehler, T. L. (1993, January). Automated whole sky imaging systems for cloud field assessment. In Fourth Symposium on Global Change Studies, American Meteorological Society (pp. 228-231).

Shields, J. E., Karr, M. E., Burden, A. R., Johnson, R. W., Mikuls, V. W., Streeter, J. R., & Hodgkiss, W. S. (2009). *Research toward Multi-site Characterization of Sky Obscuration by Clouds*. SCRIPPS INSTITUTION OF OCEANOGRAPHY LA JOLLA CA MARINE PHYSICAL LAB.

Sulaiman M, Hlaing W, Wahab M, Sulaiman Z. Analysis of residuals in daily solar radiation time series. Renewable Energy 1997.

West, S. R., Rowe, D., Sayeef, S., & Berry, A. (2014). Short-term irradiance forecasting using skycams: Motivation and development. *Solar Energy*, *110*, 188-207.

Urquhart, B., Ghonima, M., Nguyen, D., Kurtz, B., Chow, C. W., & Kleissl, J. (2013). Sky imaging systems for short-term forecasting. Solar Energy Forecasting and Resource Assessment. Elsevier.